

## 1 Fundamental Role of Oxygen Stoichiometry in Controlling the Band 2 Gap and Reactivity of Cupric Oxide Nanosheets

3 Zachary S. Fishman,<sup>†</sup> Benjamin Rudshiteyn,<sup>‡</sup> Yulian He,<sup>§</sup> Bolun Liu,<sup>||</sup> Subhajyoti Chaudhuri,<sup>‡</sup>  
4 Mikhail Askerka,<sup>‡</sup> Gary L. Haller,<sup>†,‡</sup> Victor S. Batista,<sup>\*,‡</sup> and Lisa D. Pfefferle<sup>\*,†</sup>

5 <sup>†</sup>Department of Chemical and Environmental Engineering, Yale University, New Haven, Connecticut 06520-8286, United States

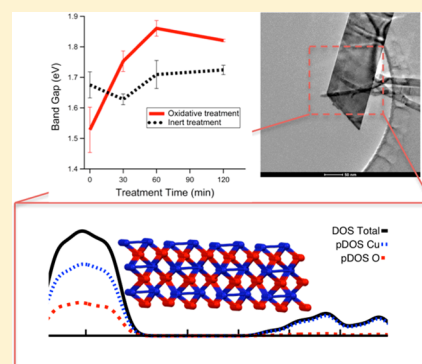
6 <sup>‡</sup>Department of Chemistry and Energy Sciences Institute, Yale University, New Haven, Connecticut 06520-8107, United States

7 <sup>§</sup>Department of Chemistry, Nankai University, Tianjin 300071, China

8 <sup>||</sup>Department of Mechanical Engineering, Yale University, New Haven, Connecticut 06520-8286, United States

9 **S** Supporting Information

10 **ABSTRACT:** CuO is a nonhazardous, earth-abundant material that has exciting  
11 potential for use in solar cells, photocatalysis, and other optoelectronic applications.  
12 While progress has been made on the characterization of properties and reactivity of  
13 CuO, there remains significant controversy on how to control the precise band gap  
14 by tuning conditions of synthetic methods. Here, we combine experimental and  
15 theoretical methods to address the origin of the wide distribution of reported band  
16 gaps for CuO nanosheets. We establish reaction conditions to control the band gap  
17 and reactivity via a high-temperature treatment in an oxygen-rich environment.  
18 SEM, TEM, XRD, and BET physisorption reveals little to no change in  
19 nanostructure, crystal structure, or surface area. In contrast, UV–vis spectroscopy  
20 shows a modulation in the material band gap over a range of 330 meV. A similar  
21 trend is found in H<sub>2</sub> temperature-programmed reduction where peak H<sub>2</sub>  
22 consumption decreases with temperature. Calculations of the density of states  
23 show that increasing the oxygen to copper coverage ratio of the surface accounts for  
24 most of the observed changes in the band gap. An oxygen exchange mechanism, supported by <sup>18</sup>O<sub>2</sub> temperature-programmed  
25 oxidation, is proposed to be responsible for changes in the CuO nanosheet oxygen to copper stoichiometry. The changes induced  
26 by oxygen depletion/deposition serve to explain discrepancies in the band gap of CuO, as reported in the literature, as well as  
27 dramatic differences in catalytic performance.



## 28 ■ INTRODUCTION

29 In recent years much effort has gone toward raising the  
30 efficiencies of solar cells and photocatalytic processes.  
31 Researchers investigating materials such as GaAs, CdTe, InP,  
32 and others have shown results as good or better than their  
33 silicon counterparts.<sup>1</sup> The main limitation of silicon is its band  
34 gap, the minimum threshold energy a photon must possess  
35 before it can be absorbed, which placed at ~1.07 eV causes it to  
36 miss long-wavelength light (>1100 nm).<sup>2</sup> Indeed, one reason  
37 these new materials work so well is because of their amenable  
38 band gap for solar light absorption according to the Shockley–  
39 Queisser limit.<sup>3</sup> The drawback, however, of many of these novel  
40 materials is their high toxicity and the fact that they contain  
41 rare-earth elements, which together serve to limit the  
42 sustainability of a device over its lifetime.<sup>4</sup> In the case of  
43 photocatalysis there are even more stringent constraints placed  
44 on a material; not only must its band gap be amenable to light  
45 absorption in the solar spectrum but also it must overcome the  
46 electrochemical barriers for a given reaction.<sup>5</sup> Other properties  
47 such as catalyst stability, toxicity, and abundance must also be  
48 considered.

49 Cupric oxide (CuO) is a p-type semiconductor that has been  
50 the subject of growing interest recently in the solar community  
51 as well as other fields including batteries,<sup>6</sup> sensors,<sup>7,8</sup> catalysis,<sup>9</sup>  
52 supercapacitors,<sup>10,11</sup> and others. In solar cells, CuO nanorod  
53 arrays have been used as an anode with TiO<sub>2</sub>,<sup>12</sup> as a barrier  
54 layer with ZnO,<sup>13</sup> and as an active layer with C<sub>60</sub>.<sup>14</sup> Rajeshwar  
55 et al. found that differently synthesized CuO–Cu<sub>2</sub>O nanorod  
56 arrays could photoelectrocatalytically convert CO<sub>2</sub> to meth-  
57 anol.<sup>15</sup> Though it was also found that the different synthesis  
58 conditions led to different efficiencies, it is still unclear what  
59 material properties led to these observed differences in  
60 performance.

61 Though much work has been done using CuO for specific  
62 applications, basic material properties remain poorly defined,  
63 most prominently band gap. The band gap of bulk copper oxide  
64 has been reported to be between 1.2 and 2.1 eV.<sup>10,16–19</sup> The  
65 band gap of nano-CuO has been reported to be as high as 4.03  
66 eV.<sup>20</sup> Additional inconsistencies exist between experimental  
67 results and theoretical models as to whether the transition is 67

Received: May 24, 2016

68 direct or indirect. Many researchers have synthesized a wide  
69 range of CuO nanostructures through a variety of methods and  
70 noted how the band gap changes with different structures.<sup>10</sup>  
71 Though it is not unusual for band gap to change with nanosize  
72 and structure, this explanation alone does not sufficiently  
73 account for the wide range of band gaps reported in the CuO  
74 system. First, strong quantum confinement effects for CuO  
75 nanoparticles with crystallite sizes between 11 and 20 nm varied  
76 the band gap in a range of only 4.03–3.72 eV.<sup>20</sup> Second, the  
77 argument of different nanoshapes, rather than size, was shown  
78 only to vary the band gap in a range of 1.371–1.447 eV.<sup>21</sup>  
79 Third, large differences in band gap are reported even in the  
80 case of bulk (non-nano) CuO. This unexplained large variance  
81 in reported values suggests that the band gap of CuO may be  
82 highly susceptible to small material changes and therefore  
83 tunable.

84 2D CuO nanosheets were chosen for this study for multiple  
85 reasons: (1) CuO as a material has shown promise in a number  
86 of applications due to its low toxicity, high abundance, and  
87 good electrical and catalytic properties, etc. (2) A fundamental  
88 unanswered scientific question exists as to why CuO has such a  
89 large variation in reported band gaps even for the bulk. (3)  
90 Two-dimensional nanosheet structures are often more  
91 amenable to photocatalytic and solar cell applications because  
92 of their increased surface area, face-dependent activity and  
93 selectivity, more forgiving density of states, and ease of  
94 compositing through sheet–sheet stacking. Finally, while  
95 much research has been done on 0D and 1D there are only a  
96 few reports that discuss tuning the properties of 2D materials  
97 beyond graphene systems.<sup>22,23</sup>

98 In this work, CuO nanosheets were synthesized via a simple  
99 surfactant-assisted aqueous-phase method and then annealed at  
100 350 °C in oxygen for different amounts of time. This annealing  
101 process was found to allow for the fine-tuning of the material's  
102 band gap as well as imbuing it with an increased reactivity.  
103 Theoretical tight-binding calculations show that oxygen cover-  
104 age and arrangement strongly influence much of the band gap.  
105 A mechanism is finally proposed for this nondegradative  
106 process and supported with evidence from isotopic oxygen  
107 studies.

## 108 ■ METHODS

109 **Experimental Section.** All chemicals used here were purchased  
110 from Sigma-Aldrich with purity  $\geq 97\%$ . All gases used were ultrahigh  
111 purity obtained from Airgas.

112 **Synthesis of Cupric Oxide Nanosheets.** Cupric oxide nanosheets  
113 were synthesized as per the following protocol:<sup>39</sup>

114 First, 120 g of sodium hydroxide and 22 g of hexadecyltrimethy-  
115 lammonium bromide (CTAB) were dissolved in 900 mL of deionized  
116 water and heated to 60 °C under magnetic stirring. In a separate  
117 beaker, 3.4 g of copper(II) nitrate trihydrate was added to 100 mL of  
118 deionized water. Once dissolved the contents of the copper nitrate  
119 solution were added to the first solution such that the final  
120 concentrations of all species were 3 M NaOH, 60 mM CTAB, and  
121 14 mM Cu(NO<sub>3</sub>)<sub>2</sub>, respectively. The solution was held at a constant  
122 temperature of 60 °C for 1 h and then removed from heating and  
123 filtered. The black precipitate was washed with excess deionized water  
124 and ethanol. To remove any remaining CTAB the samples were then  
125 calcined at 250 °C in air for 3 h and then finely ground with mortar  
126 and pestle before further treatment or characterization.

127 **Oxidative and Inert Heat Treatment.** The properties of cupric  
128 oxide nanosheets were tuned using a flow reactor as follows. Omega  
129 FMA-A2404, FMA-A2402-SS, and FMA5504 mass flow controllers  
130 were calibrated and used for all gas flow experiments. ColeParmer  
131 Digi-Sense R/S temperature controllers with Omega K-type

thermocouples were calibrated and used for all temperature  
monitoring and controlling.

An appropriate amount of cupric oxide nanosheets (50–150 mg)  
was loaded into a straight quartz tube reactor and sealed within the  
setup. A stream of 100% oxygen was flowed over the sample at a rate  
of 100 mL/min. An hour was allowed for the flow to stabilize, after  
which point heating commenced. Under the previously mentioned gas  
flow conditions the sample was heated from room temperature to 100  
°C over a period of 5 min and then heated from 100 to 350 °C over a  
period of 15 min. The sample was then left at 350 °C for a period of  
30, 60, or 120 min depending on the treatment. After treatment, the  
sample was allowed to cool naturally under 100% oxygen flow and  
then subsequently removed for analysis.

Inert treatments were conducted under similar conditions except  
nitrogen was used as the flow gas instead of oxygen.

**Scanning Electron Microscopy (SEM), Transmission Electron  
Microscopy (TEM), and Energy-Dispersive X-ray Spectroscopy  
(EDX).** SEM images and TEM images were collected on a Hitachi  
SU-70 and FEI Tecnai Osiris, respectively, both equipped with an  
energy-dispersive X-ray detector. The acceleration voltage was 15 kV  
for SEM and 200 kV for TEM. For SEM, powder samples were  
pressed onto double-sided carbon tape, while TEM samples were  
dispersed in ethanol via sonication and then added dropwise to a holey  
carbon-coated gold grid. In both cases multiple spots were examined  
to ensure sample uniformity, and the EDX spectrum was acquired to  
verify that the structures were indeed composed of copper and oxygen.

**X-ray Diffraction (XRD).** XRD measurements were carried out on  
powder samples. Spectra were acquired from a Rigaku SmartLab X-ray  
diffractometer using Cu K $\alpha$  radiation ( $\lambda = 1.5418$  Å) with a rotating  
anode source, operated at 45 kV and 200 mA. PDXL 2 Rigaku data  
analysis software was used to obtain lattice constants and crystallite  
sizes.

**UV–Visible Spectroscopy (UV–vis).** UV–vis spectra were collected  
from an Applied NanoFluorescence, LLC model NS1 Nano-  
spectralyzer. Samples were sonicated in water until dispersed and  
then aliquoted into a 1 mL UV–visible transparent cuvette.  
Measurements were repeated three to five times per sample, and  
then a Tauc plot<sup>24</sup> was used to determine band gap. A software  
package was developed in house to automate this process as well as to  
improve interpretation consistency. The band gaps presented are the  
averages of the three to five samples, and the error bars represent the  
standard deviation of the measurements.

**BET Surface Area.** The surface area of CuO nanosheet samples was  
determined using a Quantachrome autosorb. Adsorption–desorption  
isotherms were constructed using an 11-point Brunauer, Emmett, and  
Teller (BET) measurements protocol with N<sub>2</sub> as the adsorbate.  
Typically 50–100 mg of sample was used and outgassed at 200 °C for  
3–6 h. Measurements of each sample were performed in triplicate and  
their average and standard deviation calculated.

**H<sub>2</sub> Temperature-Programmed Reduction (TPR) and <sup>18</sup>O<sub>2</sub> Temper-  
ature-Programmed Oxidation (TPO).** The TPR and isotopic oxygen  
studies were carried out in a reactor setup similar to that used for the  
O<sub>2</sub> treatments with the addition of a sampling line at the outlet leading  
to a vacuum chamber operating at 10<sup>−5</sup> to 10<sup>−7</sup> Torr containing a SRS  
RGA 100 residual gas analyzer which was used to perform real-time  
mass spectrometry measurements. For TPR, 50 mg of sample was  
loaded into a straight tube quartz reactor, and a gas stream composed  
of 10% H<sub>2</sub> gas (90% Argon) was flowed over it at a rate of 100 mL/  
min for 1 h prior to heating. Flow rates were controlled using mass  
flow controllers. Samples were then heated from room temperature to  
100 °C in 5 min and then allowed to sit at 100 °C for 5 min before  
ramping from 100 to 400 °C at a rate of 10 °C per minute. For TPO,  
50 mg of CuO nanosheets was loaded, and a gas stream composed of  
4% <sup>18</sup>O<sub>2</sub> (96% He) was flowed over the sample. The purity of the <sup>18</sup>O  
with respect to <sup>16</sup>O was reported as 99:1. The sample was then heated  
to 450 °C at a rate consistent with the TPR method. Again, the outlet  
gas was measured using the residual gas analyzer.

**Computational.** The structure of monoclinic CuO was generated  
from a unit cell found in the literature<sup>25,26</sup> with  $a = 18.612$  Å,  $b = 200$   
13.640 Å, and  $c = 25.001$  Å with  $\alpha = 90.000^\circ$ ,  $\beta = 99.481^\circ$ , and  $\gamma = 201$

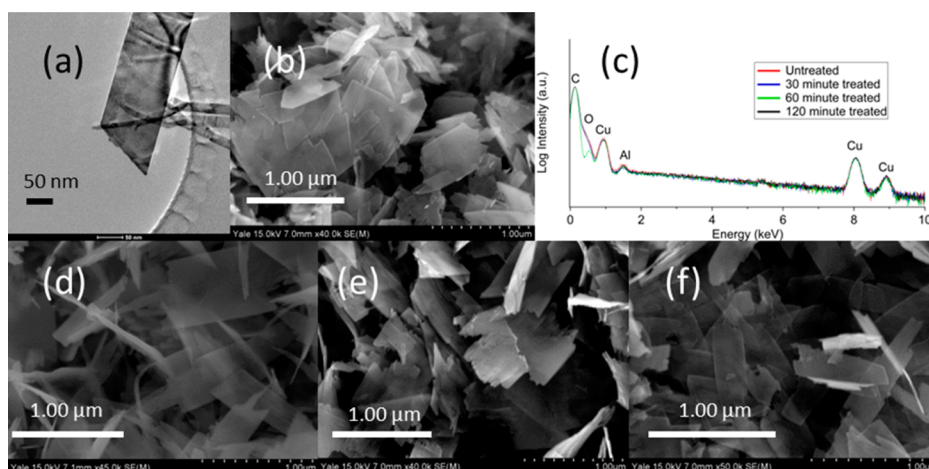


**Figure 1.** TEM (a) and SEM (b) images of untreated CuO nanosheets accompanied by EDX spectra (c) detailing its composition (copper and oxygen). The C and Al peaks are present because carbon tape was used to adhere powder samples to an aluminum stage. SEM images of 30, 60, and 120 min treated samples are presented in (d), (e), and (f), respectively.

90.000°. The slab/supercell was generated by extending the structure along the (002) plane that was most expressed by the system (Figure 2). It contained 96 units of [CuO] with four alternating layers of 32

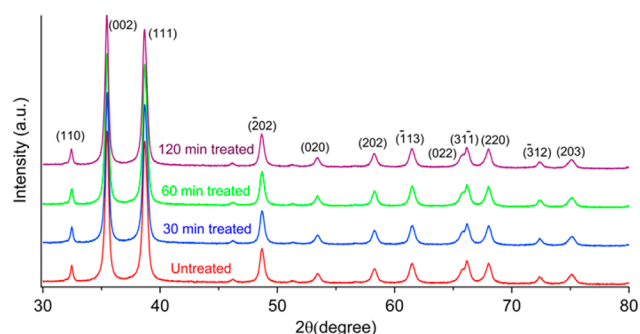


**Figure 2.** XRD spectra of CuO nanosheet 30 min (blue), 60 min (green), and 120 min (purple) treated and untreated (red) samples. Each peak is labeled with its corresponding face.

once supplied with the equilibrium geometry as described by crystallographic models or DFT methods,<sup>32</sup> as reported in this study. DFT calculations (SI, Section III) show minor surface reconstruction effects induced by changes in the level of oxygen coverage, providing robust structural models essential for an accurate description of changes in the band gap.

## RESULTS AND DISCUSSION

**Imaging.** After synthesis, all samples were imaged to determine their nanostructure. Figures 1a and 1b show a typical TEM and SEM image (respectively) of an untreated sample. Here, we see that the material is in the form of nanosheets whose dimension ranges from 250 to 1000 nm in length and width. In previous work, we have found the nanosheet range in thickness between 15 and 25 nm.<sup>53</sup> Also of note is the nonuniformity in the edges of the nanosheets, which others have cited as a result of the nanosheet growth process.

An EDX spectrum in Figure 1c provides elemental analysis of a structure found in the untreated sample and confirms it contains copper. Since carbon tape was used to adhere the sample to the stage and since this method is not sensitive enough to differentiate between the energies of carbon and oxygen, other methods (e.g., XRD) were used to confirm the material is in fact cupric oxide.

Figures 1d, 1e, and 1f show samples of copper oxide nanosheets after 30, 60, and 120 min of heat treatment at 350 °C, respectively. Here, we see that the nanosheet structure remains largely intact. Minor perturbations in the structure are, however, observable. For example, for the 120 min treated sample, there appears to be a rounding of the normally jagged edges present in the untreated sample. Indeed, for longer treatment times or for higher temperatures more extreme structural changes have been observed to occur (Figure S1). The temperature of 350 °C was chosen for this study because at higher temperatures structure loss was observed to occur too quickly.

**Crystal Structure.** X-ray diffraction (XRD) was used to determine the oxidation state and overall composition of the samples. Copper has two oxides: cuprous oxide (Cu<sub>2</sub>O) with copper having a +1 oxidation state and cupric oxide (CuO) in which copper has a +2 oxidation state. Fortunately each of these oxidation states has exactly one associated crystal structure, which for cupric oxide is monoclinic. This makes



273 XRD an ideal technique for differentiating between samples of  
274 cupric and cuprous oxide. Figure 2 shows XRD spectra  
275 collected for treated and untreated samples.

276 Peaks corresponding to each crystal face are labeled in Figure  
277 2, and the lattice parameters of each are presented in Table 1.

**Table 1. Lattice Parameters and Crystallite Sizes for the CuO Nanosheets in Figure 2**

time treated (min)	<i>a</i> (Å)	<i>b</i> (Å)	<i>c</i> (Å)	$\beta$ (deg)	crystallite size (Å)
untreated	4.6921	3.4287	5.1380	99.54	223 ± 28
30	6.6925	3.4275	5.1395	99.57	192 ± 62
60	4.6947	3.4276	5.1385	99.50	181 ± 51
120	4.6936	3.4218	5.1406	99.44	181 ± 56

278 Lattice constants were found to be approximately 4.69, 3.43,  
279 and 5.14 Å for *a*, *b*, and *c*, respectively, and approximately 95°  
280 for  $\beta$  ( $\alpha = \gamma = 90^\circ$ ). The crystallite size was found to be  
281 approximately 200 Å which agrees with our previous studies<sup>39</sup>  
282 as well as empirical thickness calculations derived from surface  
283 area (*vide infra*).

284 The lattice parameter values agree very well with literature  
285 values of CuO, and little change was observed for these values  
286 as a function of treatment time, which would suggest that the  
287 oxidative treatment has little to no effect on crystal structure or  
288 on the overall oxidation state. No cuprous oxide was detected  
289 in any sample.

290 Also of note is the increased amplitude of the peak associated  
291 with the (002) plane with respect to the other peaks compared  
292 to bulk (non-nano) CuO, which suggests an overexpression of  
293 the (002) plane in these CuO nanosheet samples, which other  
294 researchers have noted exhibits increased catalytic performance  
295 in the case of CO oxidation.<sup>10,54</sup> The high reactivity of this  
296 plane may leave it more susceptible to alterations such as by  
297 introducing or annealing away defects or by functionalization of  
298 its surface. Below, we will demonstrate how changes to the  
299 surface of CuO nanosheets lead to differences in optical  
300 properties and reactivity.

301 **Optical Properties.** UV–visible spectroscopy was used to  
302 test differences in the optical properties of the CuO nanosheet  
303 samples. This technique has been extensively implemented in  
304 semiconductor research to determine a material's band gap.  
305 Here, absorbance spectra of CuO nanosheets dispersed in  
306 deionized water were collected and plotted as a function of  
307 wavelength, which were then converted into Tauc plots<sup>24</sup> via  
308 the following transformation

$$(h\nu\alpha)^{1/n} = A(h\nu - E_g) \quad (1)$$

310 where *h* is Planck's constant;  $\nu$  is the frequency of light;  $\alpha$  is the  
311 absorption coefficient; *n* is 1/2 for a direct band gap transition  
312 and 2 for an indirect band gap transition; *A* is a proportionality  
313 constant; and  $E_g$  is band gap. The band gap of a material may  
314 be determined by constructing a Tauc plot, that is by plotting  
315  $(\alpha E_{\text{phot}})^2$  against  $E_{\text{phot}}$ , where  $E_{\text{phot}}$  is the energy of a photon  
316 ( $h\nu$ ). Linear extrapolation of each sample's trace down to the  
317  $E_{\text{phot}}$  axis should yield the value of the band gap of the materials.  
318 Software was developed in house to automate this process and  
319 increase the consistency of the band gap determined for a given  
320 data set.

321 Example Tauc plots of each treatment are depicted in Figure  
322 S2, and calculated band gaps for each sample are plotted in  
323 Figure 3 as a function of treatment time. It was found that CuO

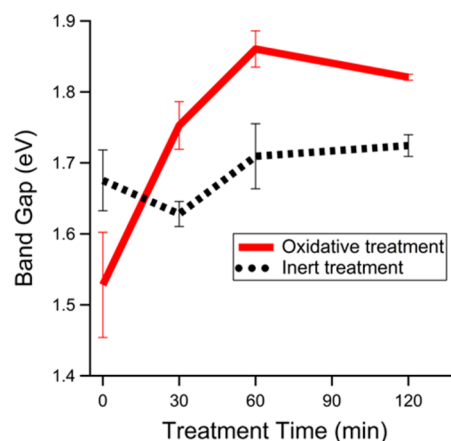


**Figure 3.** Band gaps of treated and untreated CuO nanosheet samples in an oxidative treatment (red solid) and with an inert treatment (black dotted). Each data point is an average over five measurements, and the error bars represent the standard deviation.

324 nanosheets exhibit a direct band gap transition of 1.53 eV in the  
325 untreated sample. It was subsequently found that 30 min of  
326 oxidative treatment increased the band gap to 1.75 eV and 60  
327 min to 1.86 eV. However, after 120 min of treatment, the band  
328 gap started to once again decrease, down to 1.82 eV. The  
329 standard deviations for all of these measurements were between  
330 26 and 74 meV.

331 A separate sample of CuO nanosheets was treated at 350 °C  
332 for 30, 60, and 120 min in N<sub>2</sub> gas. Under these inert treatment  
333 conditions we observe a much smaller change in the band gap  
334 from 1.68 to 1.63 eV to 1.71 to 1.72 eV for untreated, 30, 60,  
335 and 120 min samples, respectively. We posit that the oxidative  
336 treatment results in more pronounced band gap changes due to  
337 increased O:Cu coverage of the CuO nanosheet surface. During  
338 inert treatment, no oxygen addition is possible from the gas  
339 phase though small band gap changes may be a result of oxygen  
340 and/or copper rearrangement from atoms already present on  
341 the surface. We also observe batch to batch differences in the  
342 band gap for untreated CuO nanosheets. In Figure 2, the  
343 untreated sample in the oxidative and inert series has a band  
344 gap of 1.53 and 1.68 eV, respectively, which we also attribute to  
345 a difference in the amount and distribution of surface oxygen  
346 atoms. Below, we use theoretical calculations in conjunction  
347 with experimental results to support these assertions as well as  
348 to demonstrate how differences to surface oxygen sites  
349 influence reducibility.

350 **Theoretical Calculations.** We have modeled the crystallo-  
351 graphic structure of CuO, using tight-binding methods as  
352 described in the Computational methods section, to explore  
353 how the oxidative treatment changes the sample at a molecular  
354 level. Figure 4 shows the total density of states (DOS) for  
355 model 2D CuO nanosheets as well as the projected density of  
356 states (pDOS) for Cu and O atoms. For an ideal CuO structure  
357 with 1:1 ratio of Cu:O (Figure 4a), the band gap is 1.05 eV, in  
358 reasonable agreement with other theoretical calculations<sup>55</sup> and  
359 acceptably close to the band gap value found in Table 2 for the  
360 untreated sample. Typically, band gaps obtained at this level of  
361 theory underestimate the experimental band gaps by a few 100  
362 meV.<sup>55</sup> To simulate an oxygen-rich surface, 8, 16, and 24 Cu  
363 atoms were removed from the top layer, as shown in Figures  
364 4b, 4c, and 4d, respectively. Cu depletion resulted in a band gap  
365 increase, from 1.05 to 1.26 eV and 1.42 and 1.75 eV for the 0, 8,  
366 16, and 24 Cu atoms removed, respectively. Conversely 366

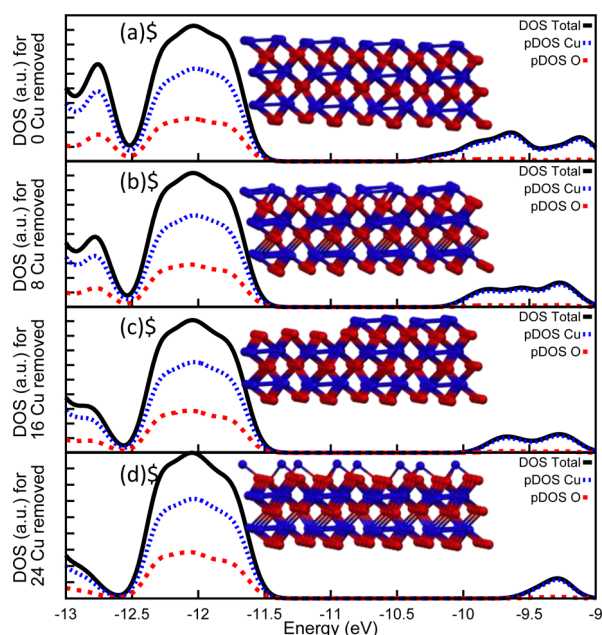


**Figure 4.** Total DOS (black) and pDOS (blue = Cu, red = O) for CuO (geometries shown as in insets) in various states of removal from the top copper layer in a “regular” fashion where the first atom is deleted in the first vertical row, the second atom is deleted in the second vertical row, etc. The pristine slab is given in (a). 8, 16, and 24 Cu atoms are deleted in (b), (c), and (d), respectively. Color code: blue = Cu, red = O.

**Table 2. Mean Values for the Band Gap of Each CuO Nanosheet Sample**

time treated (min)	band gap (eV)	
	oxidative	inert
untreated	1.53 ± 0.074	1.68 ± 0.043
30	1.75 ± 0.033	1.63 ± 0.018
60	1.86 ± 0.026	1.71 ± 0.046
120	1.82 ± 0.042	1.72 ± 0.015

nanosheets becomes relatively more oxygen rich when exposed to the oxidative treatment, which is consistent with the observed increase in band gap. Similar results were obtained for CuO nanowires where adsorption of water to the (111) surface resulted in a wider band gap.<sup>56</sup>

The rearrangement of oxygen on the surface was also investigated using molecular modeling to determine its impact on the CuO nanosheet band gap. Such calculations effectively model the effect of surface rearrangement upon oxidation or reduction. In Figure 5a, 16 Cu atoms were removed from the

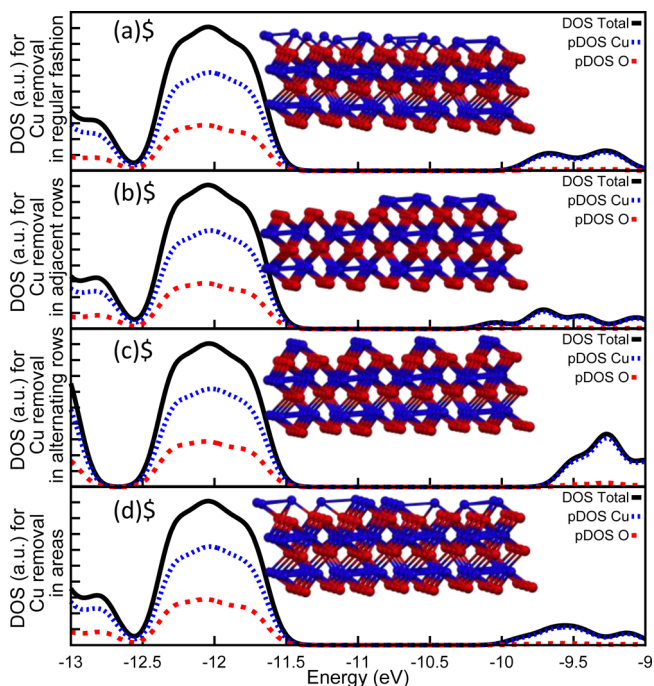


**Figure 5.** Total DOS (black) and pDOS (blue = Cu, red = O) for CuO (geometries shown as in insets) in various states of removal of 16 Cu atoms from the top layer. For the “regular fashion” pattern of removal (a) the first atom of the first vertical row was deleted, the second atom of the second row, etc. In (b) adjacent rows of Cu atoms were deleted. In (c) alternating rows were deleted. “Areas” (d) refer to roughly hexagonal portions deleted from the surface. Color code: blue = Cu, red = O.

bottom layer, but the pattern of removal was varied. In Figure 5a, the atoms were removed in a regular fashion, that is, the first Cu atom of the first row, the second Cu atom of the second row, etc. which was also the method of removal in Figure 4. For comparison, the adjacent rows of Cu atoms were removed (Figure 5b) resulting in a band gap of 1.16 eV. In Figure 5c, alternative rows were removed resulting in a band gap of 1.67 eV. In Figure 5d, hexagonal areas of Cu atoms were removed yielding a band gap of 1.39 eV. The structures used are displayed in the inset of each DOS plot. Analogous plots with oxygen atoms removed can be found in Figure S4. These results are also summarized in Table 3 and Table S1. Diffuse removal of Cu atoms such as in (a) or (d) yielded structures with very similar band gaps, while more ordered removal patterns such as those found in (b) and (c) resulted in band gaps that were much more varied. We posit that by removing atoms in such a clustered configuration a new interface is created between two separate materials. These metal–metal oxide interfaces could provide a collection of mid band gap of energy states in between the more populated band edges, hence

**Table 3. Values for the Band Gap of Each CuO Model Given in Figures 4 and 5**

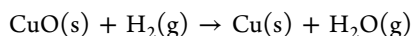
Cu atoms removed	arrangement	valence band (eV)	conduction band (eV)	band gap (eV)
0	regular	−11.4	−10.35	1.05
8	regular	−11.39	−10.13	1.26
16	regular	−11.38	−9.96	1.42
16	adjacent	−11.38	−10.22	1.16
16	alternating	−11.39	−9.72	1.67
16	areas	−11.38	−9.99	1.39
24	regular	−11.37	−9.62	1.75

and the Supporting Information. We find that changes in the band gap largely result from a change in the conduction band of the material, rich in Cu d states, increasing in the case of Cu removal and decreasing in the case of O removal. The results of our theoretical models are consistent with the experimental conclusion that the band gap of CuO increases with increasing surface oxygen coverage. It is expected that the surface of CuO

lowering the apparent band gap of the material. We selected to remove 16 Cu atoms to test arrangement effects because it results in a Cu:O ratio of 1:1.20 which, as will be shown below, is close to the ratio measured experimentally for CuO nanosheets.

These theoretical results also help explain changes found in CuO nanosheets treated in an inert environment. Slight increases and decreases in band gap found can be attributed to the rearrangement of oxygen atoms on the surface. For example, structures may transition from a “regular” distribution to an “alternating” arrangement, which would increase the band gap, then to an “adjacent” configuration, which would decrease the band gap, or to the “areas” structure, which would keep the band gap relatively constant. Based on the experimental results the latter is more likely since little to no change in band gap is observed.

**Reactivity.** In this section, we demonstrate how increases in the band gap of CuO nanosheets correlate with increases in reactivity. Hydrogen oxidation was used as a probe reaction to quantify differences in reducibility. The reduction of CuO in hydrogen gas is a well-studied process.<sup>42</sup> CuO, rather than being reduced sequentially to Cu<sub>2</sub>O and then to Cu, has been shown to reduce directly to Cu according to the following reaction



First, the surface areas of all samples were measured in triplicate using 11 point BET N<sub>2</sub> physisorption. The mean of each sample along with the standard deviation is listed in Table 4. All

**Table 4. Mean Surface Area Values and Estimated Nanosheet Thicknesses for Each CuO Sample Are Presented**

time treated (min)	surface area (m <sup>2</sup> /g)	average calculated thickness (nm)
untreated	23.05 ± 0.66	13.75
30	20.79 ± 1.84	15.25
60	21.89 ± 0.41	14.48
120	21.87 ± 1.06	14.49

samples fell within a range of 20–24 m<sup>2</sup>/g with very little difference in surface area between them. Interestingly, surface area can be used to calculate the average thickness of the nanosheets present within the sample using eq 2.

$$\bar{t} = \frac{2}{\sigma\rho} \quad (2)$$

where  $\bar{t}$  is the average thickness of a CuO nanosheet;  $\sigma$  is the surface area per unit mass of the sample; and  $\rho$  is the density of CuO, which is  $6.31 \times 10^6$  g/m<sup>3</sup>. An analogue analysis is done by Weiber et al. for 0D nanoparticles;<sup>57</sup> however, since no such report exists for 2D materials (to the best of our knowledge) a short derivation is included in the Supporting Information, Section II.

Thicknesses for each sample are presented in Table 4. These values are likely an underestimation of the actual thickness since roughness and jagged edges, which are visible from the SEM images in Figure 1, increase the surface area. Interestingly these values are in agreement with crystallite sizes obtained from XRD. Together with the SEM images shown in Figure 1, these data reinforce the claim that the treatment has not impacted the structure of the CuO nanosheets

H<sub>2</sub> TPR was performed on oxidized CuO nanosheets, as shown in Figure 6. Here 50 mg of treated and untreated

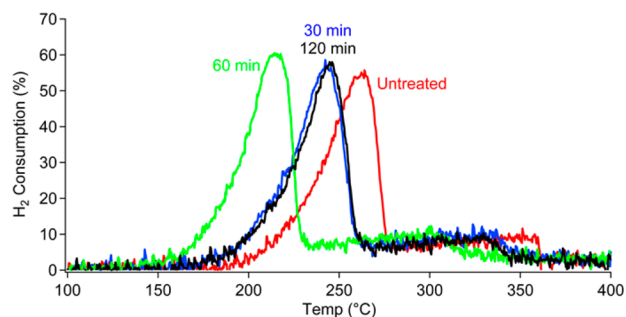


**Figure 6.** Mass spectrum-derived percent consumption of H<sub>2</sub> for 50 mg of each sample at different temperatures with tabular values given in Table 5.

samples were heated in 10% H<sub>2</sub> gas (in an Ar atmosphere) flow from 100 to 400 °C, and the composition of the outlet gas stream was assessed using mass spectrometry. Since no gaseous oxygen is present for this reaction, all hydrogen that is consumed is being oxidized by the CuO nanosheets, which degrades the CuO nanosheets so that neither structure nor composition is preserved. However, differences in the initial state of the nanosheets affect the temperature at which the material reacts.

Percent H<sub>2</sub> consumption is given as a function of temperature in Figure 6 for each sample. At a given temperature, increased H<sub>2</sub> consumption indicates more reaction is occurring between the material and the gas. When all of the oxygen has been depleted (i.e., when all CuO has been converted to Cu) the reaction ceases, and no further H<sub>2</sub> is consumed. In Figure 6, we see that peak H<sub>2</sub> consumption temperature decreases from 261 °C for the untreated sample to 242 °C for the 30 min treated sample and to 214 °C for the 60 min sample. For the 120 min sample, the peak H<sub>2</sub> consumption temperature increases back to 244 °C. Note that this follows a similar trend to the sample’s band gap in that CuO nanosheets with higher band gap show increased reactivity with H<sub>2</sub> (as indicated by a lower reaction temperature) and vice versa, which indicates that there is a correlation between the band gap and reactivity of CuO nanosheets so that by tuning one the other is also tuned, which makes it possible to predict *a priori* how changes in the band gap of CuO nanosheets will impact its reactivity.

Values for total H<sub>2</sub> consumed are listed in Table 5. These values were derived by integrating the H<sub>2</sub> consumption curves and using the prior knowledge of the quantity of H<sub>2</sub> flowed during the experiment. Equation 3 outlines this explicitly.

$$\frac{\text{Peak Area}}{\text{Total Area}} = \frac{\text{H}_2 \text{ Consumed}}{\text{Total H}_2 \text{ Flowed}} \quad (3)$$

**Table 5. Peak Consumption Temperatures<sup>a</sup>**

time treated (min)	peak H <sub>2</sub> consumption temp. (°C)	total H <sub>2</sub> consumed (mmol)	Cu:O
untreated	261	0.794	1:1.26
30	242	0.761	1:1.21
60	214	0.777	1:1.23
120	244	0.775	1:1.24

<sup>a</sup>These temperatures follow a trend similar to the material band gap. Total H<sub>2</sub> consumed was found by integrating each peak and using the ideal gas law. Cu:O ratios were determined assuming 1 mol of H<sub>2</sub> per atom of O present in the material.



where Total Area is the area below the line  $y = 100\%$  from 100 to 400 °C or  $100 \times 300 = 30\,000$  which is the theoretical maximum consumption. The total  $H_2$  flowed refers the total amount of moles calculated using a flow rate of 10 mL/min (10% of a 100 mL/min stream) and the ideal gas law. From the above reaction, 1 molecule of  $H_2$  is consumed per oxygen atom of CuO. Therefore, these values also serve as a measure of oxygen content for these structures. The theoretical amount of O atoms in 50 mg of sample with a 1:1 Cu:O ratio is 0.630 mmol. In this study we find that all CuO nanosheet samples had increased amounts of oxygen. As depicted in Table 4 the Cu:O ratio goes from 1:1.26 in the untreated sample to 1:1.21 to 1:1.24 to 1:23. Thus, all CuO nanosheets studied here have an excess amount of oxygen, which would explain why the band gaps do not match a theoretical pristine slab of CuO where the ratio for Cu:O is 1:1. This trend is not identical to the trend in band gap in that the untreated sample, though it contains the most oxygen, does not have the highest band gap. In the treated samples, however, the oxygen amount does follow the trend of band gap. Based on our theoretical calculations, we conclude that the surface oxygen atoms in the untreated sample are more dispersed than the treated samples, which corroborates the hypothesis made in the previous section that the solution synthesized CuO nanosheets exist in a different configuration, and with heat treatment these structures can rearrange, changing their band gap. More robust spectroscopic methods may reveal that the surface of untreated CuO nanosheets contains more hydroxyl groups that likely affect the band gap in different ways, as suggested in the literature,<sup>58,59</sup> which is beyond the scope of this investigation.

$H_2$  TPR was also performed on a commercial sample of CuO, and it was found that it contained only 3.9% more oxygen (Figure S5). The high surface-to-bulk ratio of CuO nanosheets suggests that a large amount of additional oxygen lies on the surface of the material, which would explain why the band gaps reported in this work are slightly higher than the most commonly cited value of 1.4 eV.

To further support the hypothesis that oxygen from the gas phase is interacting with the material and vice versa,  $^{18}O$  temperature-programmed oxidation was performed on untreated CuO nanosheets. Figure 7 shows the production of  $^{18,16}O_2$  as a function of temperature over untreated CuO nanosheets in the presence of  $^{18}O$ .

At approximately 325 °C there is an onset of production of  $^{18,16}O_2$ . Since the atmosphere is the only source of  $^{18}O$  atoms (in the form of  $^{18}O_2$ ) and CuO nanosheets are the only source of  $^{16}O$  atoms, the production of  $^{18,16}O_2$  molecules must be a result of oxygen exchange occurring between the nanosheets

and the gas. This mechanism similar to Mars–Van Krevelin catalysts<sup>60</sup> is indicative of increased oxygen mobility in the material. We posit that this phenomenon might also be the mechanism of structural degradation in nanosheet samples heated over long time periods around this temperature (Figure S1). Thus, we conclude that the band gap and reactivity changes are a direct result of this oxygen mobility and exchange.

In analogous systems, such as carbon nanotubes, surface oxygen groups impact properties such as toxicity, reactivity, and point of zero charge.<sup>61</sup> Additionally, others have noted the correlation between band gap and catalytic performance in metal oxide systems.<sup>62</sup> Here, we find that the total amount of surface oxygen as well as its distribution affect the band gap and hydrogen oxidation activity of CuO nanosheets. We also find that these optical and catalytic properties may be tuned through varying the calcination condition.

## CONCLUSIONS

We have elucidated the fundamental role that surface oxygen deposition plays in tuning the band gap and reactivity of CuO nanosheets, an earth-abundant, nonhazardous material, useful in the fields of solar energy technology and photocatalysis. We demonstrated that the band gap of CuO nanosheets can be controlled in a range of 1.53–1.86 eV through a mild oxidative heat treatment. We found that the reactivity of the nanosheets improves upon increasing the band gap, as evidenced by  $H_2$  TPR. The observed changes in band gap and reactivity are directly correlated with changes in surface oxygen coverage, as supported by our theoretical analysis. Calculations of the DOS for a series of model CuO nanosheets show that structures with increased surface oxygen atoms have larger band gaps. Additionally, the band gaps of models with more ordered arrangements varied widely from those of more diffuse arrangements. Finally, through isotopic oxygen TPO, we demonstrate that oxygen exchange is indeed occurring between the gas phase and the solid during the oxidative heat treatments at 350 °C. We hypothesize that the sensitivity to surface oxygen vacancies is an important contributing factor for the wide range of values of CuO band gaps reported in the literature.

## ASSOCIATED CONTENT

### Supporting Information

The Supporting Information is available free of charge on the ACS Publications website at DOI: 10.1021/jacs.6b05332.

SEM image showing the effects that long heat treatments have on CuO nanosheets, namely, that nanostructure degradation begins with the smoothing of the material's jagged edges, mass spectrometry data for  $H_2$  TPR of commercial CuO showing the percent of  $H_2$  consumed at any given temperature, derivation of eq 2, and coordinates for structures used for the theoretical calculations (PDF)

## AUTHOR INFORMATION

### Corresponding Authors

\*victor.batista@yale.edu

\*lisa.pfefferle@yale.edu

### Notes

The authors declare no competing financial interest.

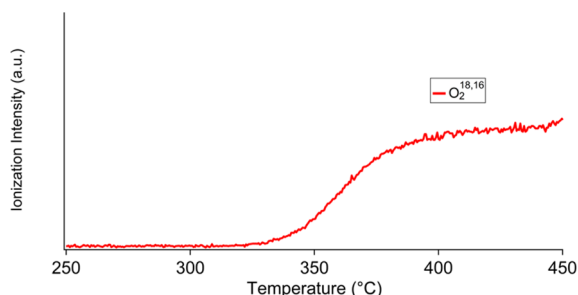


**Figure 7.** Mass spectrum of  $^{18,16}O_2$  for the reaction of CuO nanosheets (untreated) heated in the presence of isotopic oxygen gas ( $^{18}O_2$ ).

## 594 ■ ACKNOWLEDGMENTS

595 Z.S.F., Y.H., B.L., G.L.H., and L.D.P. would like to graciously  
596 thank the generous support of Army Research Laboratory for  
597 funding this research under ARO 517 grant No. 64935-MS and  
598 would like to thank the YINQE and CRISP facilities for  
599 providing access to assistance with TEM, SEM, and XRD  
600 instruments. V.S.B. acknowledges funding from the Argonne-  
601 Northwestern Solar Energy Research (ANSER) Center, an  
602 Energy Frontier Research Center funded by the U.S.  
603 Department of Energy, Office of Science, Office of Basic  
604 Energy Sciences under Award Numbers DE-PS02-08ER15944.  
605 V.S.B. also acknowledges high performance computing time  
606 from NERSC and from the Yale University Faculty of Arts and  
607 Sciences High Performance Computing Center, whose  
608 acquisition was partially funded by the National Science  
609 Foundation under grant number CNS08-21132. B.R. acknowl-  
610 edges support from the National Science Foundation Graduate  
611 Research Fellowship under Grant No. DGE-1122492. Finally,  
612 we would like to acknowledge the guidance of Dr. Charles  
613 McEnally in designing and operating reactor setups as well as  
614 other experimental systems and Mikhail Askerka and Dr. Svante  
615 Hedström for their advice on the theoretical calculations.

## 616 ■ REFERENCES

- 617 (1) Green, M. A.; Emery, K.; Hishikawa, Y.; Warta, W.; Dunlop, E. D.  
618 *Prog. Photovoltaics* **2015**, *23*, 1.  
619 (2) Wu, C.; Crouch, C. H.; Zhao, L.; Carey, J. E.; Younk, R.;  
620 Levinson, J. A.; Mazur, E.; Farrell, R. M.; Gothoskar, P.; Karger, A.  
621 *Appl. Phys. Lett.* **2001**, *78*, 1850.  
622 (3) Shockley, W.; Queisser, H. J. *J. Appl. Phys.* **1961**, *32*, 510.  
623 (4) Hardman, R. *Environ. Health Perspect.* **2006**, *114*, 165.  
624 (5) Rajeshwar, K. In *Encyclopedia of Electrochemistry*; Wiley-VCH  
625 Verlag GmbH & Co. KGaA: 2007.  
626 (6) Gao, X.; Bao, J.; Pan, G.; Zhu, H.; Huang, P.; Wu, F.; Song, D. J.  
627 *Phys. Chem. B* **2004**, *108*, 5547.  
628 (7) Chen, W.; Chen, J.; Feng, Y.-B.; Hong, L.; Chen, Q.-Y.; Wu, L.-  
629 F.; Lin, X.-H.; Xia, X.-H. *Analyst* **2012**, *137*, 1706.  
630 (8) Song, J.; Xu, L.; Zhou, C.; Xing, R.; Dai, Q.; Liu, D.; Song, H.  
631 *ACS Appl. Mater. Interfaces* **2013**, *5*, 12928.  
632 (9) Dow, W.-P.; Wang, Y.-P.; Huang, T.-J. *J. Catal.* **1996**, *160*, 155.  
633 (10) Zhang, Q.; Zhang, K.; Xu, D.; Yang, G.; Huang, H.; Nie, F.; Liu,  
634 C.; Yang, S. *Prog. Mater. Sci.* **2014**, *60*, 208.  
635 (11) Zhang, X.; Shi, W.; Zhu, J.; Kharistal, D. J.; Zhao, W.; Lalia, B.  
636 S.; Hng, H. H.; Yan, Q. *ACS Nano* **2011**, *5*, 2013.  
637 (12) Anandan, S.; Wen, X.; Yang, S. *Mater. Chem. Phys.* **2005**, *93*, 35.  
638 (13) Raksa, P.; Nilphai, S.; Gardchareon, A.; Chooipun, S. *Thin Solid*  
639 *Films* **2009**, *517*, 4741.  
640 (14) Sun, S.; Zhang, X.; Zhang, J.; Wang, L.; Song, X.; Yang, Z.  
641 *CrystEngComm* **2013**, *15*, 867.  
642 (15) Rajeshwar, K.; de Tacconi, N. R.; Ghadimkhani, G.;  
643 Chanmanee, W.; Janáky, C. *ChemPhysChem* **2013**, *14*, 2251.  
644 (16) Marabelli, F.; Parravicini, G.; Salghetti-Drioli, F. *Phys. Rev. B:*  
645 *Condens. Matter Mater. Phys.* **1995**, *52*, 1433.  
646 (17) Ogwu, A.; Darma, T.; Bouquerel, E. *J. Achiev. Mater. Manuf. Eng.*  
647 **2007**, *24*, 172.  
648 (18) Ray, S. C. *Sol. Energy Mater. Sol. Cells* **2001**, *68*, 307.  
649 (19) Hardee, K. L.; Bard, A. J. *J. Electrochem. Soc.* **1977**, *124*, 215.  
650 (20) Rehman, S.; Mumtaz, A.; Hasanain, S. J. *Nanopart. Res.* **2011**,  
651 *13*, 2497.  
652 (21) Yang, M.; He, J. *J. Colloid Interface Sci.* **2011**, *355*, 15.  
653 (22) Chhowalla, M.; Shin, H. S.; Eda, G.; Li, L.-J.; Loh, K. P.; Zhang,  
654 H. *Nat. Chem.* **2013**, *5*, 263.  
655 (23) Lee, H. S.; Min, S.-W.; Chang, Y.-G.; Park, M. K.; Nam, T.; Kim,  
656 H.; Kim, J. H.; Ryu, S.; Im, S. *Nano Lett.* **2012**, *12*, 3695.  
657 (24) Tauc, J.; Grigorovici, R.; Vancu, A. *Phys. Status Solidi B* **1966**,  
658 *15*, 627.  
(25) Villars, P. *CuO Crystal Structure Inorganic Solid Phases* 2014. 659  
[http://materials.springer.com/isp/crystallographic/docs/sd\\_0542121](http://materials.springer.com/isp/crystallographic/docs/sd_0542121)  
(accessed April 11, 2016). 660  
(26) Tunell, G.; Posnjak, E.; Ksanda, C. Z. *Kristallogr. - Cryst. Mater.* 661  
**1935**, *90*, 120. 662  
(27) Wolfsberg, M.; Helmholz, L. *J. Chem. Phys.* **1952**, *20*, 837. 663  
(28) Hoffmann, R. *J. Chem. Phys.* **1963**, *39*, 1397. 664  
(29) Hoffmann, R. *Solids and surfaces: a chemist's view of bonding in* 665  
*extended structures*; VCH Publishers: New York, 1988. 666  
(30) Alvarez, S. *Tables of parameters for extended Hückel calculations* 667  
**1989**. 668  
(31) Burdett, J. K. *Chemical Bonding in Solids*; Oxford University 669  
Press, 1995. 670  
(32) Lewars, E. G. *Computational chemistry: introduction to the theory* 671  
*and applications of molecular and quantum mechanics*; Springer Science 672  
& Business Media, 2010. 673  
(33) Landrum, G.; Glassey, W.; 3.0 ed.; Cornell University: 2001. 674  
(34) Rego, L. G.; Batista, V. S. *J. Am. Chem. Soc.* **2003**, *125*, 7989. 675  
(35) Abuabara, S. G.; Rego, L. G.; Batista, V. S. *J. Am. Chem. Soc.* 676  
**2005**, *127*, 18234. 677  
(36) Abuabara, S. G.; Cady, C. W.; Baxter, J. B.; Schmuttenmaer, C. 678  
A.; Crabtree, R. H.; Brudvig, G. W.; Batista, V. S. *J. Phys. Chem. C* 679  
**2007**, *111*, 11982. 680  
(37) McNamara, W. R.; Snoberger, Iii, R. C.; Li, G.; Schleicher, J. 681  
M.; Cady, C. W.; Poyatos, M.; Schmuttenmaer, C. A.; Crabtree, R. H.; 682  
Brudvig, G. W.; Batista, V. S. *J. Am. Chem. Soc.* **2008**, *130*, 14329. 683  
(38) Rego, L. G.; Silva, R. d.; Freire, J. A.; Snoberger, R. C.; Batista, 684  
V. S. *J. Phys. Chem. C* **2009**, *114*, 1317. 685  
(39) Li, C.; Koenigsmann, C.; Ding, W.; Rudsteyn, B.; Yang, K. R.; 686  
Regan, K. P.; Konezny, S. J.; Batista, V. S.; Brudvig, G. W.; 687  
Schmuttenmaer, C. A.; et al. *J. Am. Chem. Soc.* **2015**, *137*, 1520. 688  
(40) Hoffmann, R. *Rev. Mod. Phys.* **1988**, *60*, 601. 689  
(41) Rego, L. G.; Abuabara, S. G.; Batista, V. S. *J. Chem. Phys.* **2005**, 690  
*122*, 154709. 691  
(42) Cerda, J.; Soria, F. *Phys. Rev. B: Condens. Matter Mater. Phys.* 692  
**2000**, *61*, 7965. 693  
(43) MacGlynn, S. P.; Vanquickenborne, L. G.; Kinoshita, M.; 694  
Carroll, D. G. *Introduction to Applied Quantum Chemistry*; Holt 695  
Rinehart & Winston: New York, 1972. 696  
(44) Hay, P. J.; Thibault, J. C.; Hoffmann, R. *J. Am. Chem. Soc.* **1975**, 697  
*97*, 4884. 698  
(45) Hoffmann, R. *Angew. Chem., Int. Ed. Engl.* **1987**, *26*, 846. 699  
(46) Raza, H. *Phys. Rev. B: Condens. Matter Mater. Phys.* **2007**, *76*, 700  
045308. 701  
(47) Raza, H.; Bevan, K. H.; Kienle, D. *Phys. Rev. B: Condens. Matter* 702  
*Mater. Phys.* **2008**, *77*, 035432. 703  
(48) Raza, H.; Kan, E. C. *J. Comput. Electron.* **2008**, *7*, 372. 704  
(49) Jug, K. *Theor. Chim. Acta* **1980**, *54*, 263. 705  
(50) Levine, I. N. *Quantum Chemistry*; Pearson Prentice Hall, 2009. 706  
(51) Perdew, J. P. *Int. J. Quantum Chem.* **1985**, *28*, 497. 707  
(52) Heinemann, M.; Eifert, B.; Heiliger, C. *Phys. Rev. B: Condens.* 708  
*Matter Mater. Phys.* **2013**, *87*, 115111. 709  
(53) Gilbertson, L. M.; Albalghiti, E. M.; Fishman, Z. S.; Perreault, F.; 710  
Corredor, C.; Posner, J. D.; Elimelech, M.; Pfefferle, L. D.; 711  
Zimmerman, J. B. *Environ. Sci. Technol.* **2016**, *50*, 3975. 712  
(54) Huang, H.; Zhang, L.; Wu, K.; Yu, Q.; Chen, R.; Yang, H.; Peng, 713  
X.; Ye, Z. *Nanoscale* **2012**, *4*, 7832. 714  
(55) Ghijsen, J.; Tjeng, L.; Van Elp, J.; Eskes, H.; Westerink, J.; 715  
Sawatzky, G.; Czyzyk, M. *Phys. Rev. B: Condens. Matter Mater. Phys.* 716  
**1988**, *38*, 11322. 717  
(56) Hu, J.; Li, D.; Lu, J. G.; Wu, R. *J. Phys. Chem. C* **2010**, *114*, 718  
17120. 719  
(57) Weibel, A.; Bouchet, R.; Boulc', F.; Knauth, P. *Chem. Mater.* 720  
**2005**, *17*, 2378. 721  
(58) Warren, S.; Flavell, W.; Thomas, A.; Hollingworth, J.; 722  
Dunwoody, P.; Downes, S.; Chen, C. *Surf. Sci.* **1999**, *436*, 1. 723  
(59) Takita, Y.; Saito, Y.; Tashiro, T.; Hori, F. *Bull. Chem. Soc. Jpn.* 724  
**1985**, *58*, 1827. 725  
(60) Doornkamp, C.; Ponc, V. J. *Mol. Catal. A: Chem.* **2000**, *162*, 19. 726



- 728 (61) Gilbertson, L. M.; Goodwin, D. G., Jr; Taylor, A. D.; Pfefferle,  
729 L.; Zimmerman, J. B. *Environ. Sci. Technol.* **2014**, *48*, 5938.  
730 (62) Getsoian, A. B.; Zhai, Z.; Bell, A. T. *J. Am. Chem. Soc.* **2014**, *136*,  
731 13684.